Article

Ti Substitution Facilitating Oxygen Oxidation in $Na_{2/3}Mg_{1/3}Ti_{1/6}Mn_{1/2}O_2$ Cathode

Ti-substituted Mn-rich Na-ion cathodes

Chenglong Zhao, Zhenpeng Yao, Jianlin Wang, ..., Alán Aspuru-Guzik, Liquan Chen, Yong-Sheng Hu

yxlu@iphy.ac.cn (Y.L.)
aspuru@utoronto.ca (A.A.-G.)
yshu@iphy.ac.cn (Y.-S.H.)

HIGHLIGHTS

Ti-substituted P2-type $Na_{2/3}Mg_{1/3}Ti_{1/6}Mn_{1/2}O_2$ cathode is successfully prepared

The decreased Mg and Mn ordering distribution is observed in TMO_2 layers

Ti substitution facilitates charge-transfer reaction of oxygen redox

The highly stable high-voltage plateau is exhibited at ~4.1 V

Ti-substituted $Na_{2/3}Mg_{1/3}Ti_{1/6}Mn_{1/2}O_2$ exhibits a highly reversible capacity of ~230 mAh g^{-1} with a highly stable high-voltage plateau at ~4.1 V. This work demonstrates that the Ti substitution can reduce the Mg and Mn ordering in TMO_2 layers and modulate the electronic structure around Mg–, Ti–, and Mn–O bonding, which further improves electrochemical properties.

Chem

CellPress

Article

Ti Substitution Facilitating Oxygen Oxidation in Na$_{2/3}$Mg$_{1/3}$Ti$_{1/6}$Mn$_{1/2}$O$_2$ Cathode

Chenglong Zhao,[1,2,8] Zhenpeng Yao,[3,8] Jianlin Wang,[4] Yaxiang Lu,[1,2,*] Xuedong Bai,[4] Alán Aspuru-Guzik,[3,5,6,*] Liquan Chen,[1] and Yong-Sheng Hu[1,2,7,9,*]

SUMMARY

Understanding structure-property chemistry of electrodes will be greatly helpful for developing advanced Na-ion batteries (NIBs). To search for promising electrodes, we employ chemical substitution in Na$_{2/3}$TMO$_2$ (TM = transition metal) layered compounds with different stacking modes: O3-Na$_{2/3}$Mg$_{1/3}$Ti$_{2/3}$O$_2$ and P2-Na$_{2/3}$Mg$_{1/3}$Mn$_{2/3}$O$_2$. Partial Ti-substituted Na$_{2/3}$Mg$_{1/3}$Ti$_{1/6}$Mn$_{1/2}$O$_2$ enables significant improvements on electrochemical properties with respect to the stability of high-voltage plateau and total reversible capacity ($\sim$230 mAh g^{-1}). More than twice as much capacity is reserved in the high-voltage plateau area for the Ti-substituted cathode against non-Ti-substituted counterparts after the same cycles. The present work demonstrates that Ti substitution will decrease Mg and Mn ordering distribution in the pristine structure due to the intermediate size of Ti^{4+}, which further increases the structural stability during Na$^+$ deintercalculation and intercalculation. Additionally, Ti substitution leads to more localized electrons around oxygen ions in Mg–, Ti–, and Mn–O bonding, which can facilitate the charge-transfer reaction of oxygen redox. Our work provides new insights into structural chemistry on developing high-capacity, low-cost layered electrodes for NIBs.

INTRODUCTION

Na-ion batteries (NIBs) have been regarded as a promising supplement to Li-ion batteries (LIBs) because of the abundance of Na resources in the Earth's crust for the emerging grid energy storage applications.[1–3] Up to now, tremendous efforts have been made in both academia and industry to develop NIB technologies, including novel electrodes, electrolytes, and advanced characterization methods.[4–9] Among them, electrode materials draw the most attention for their intrinsic disadvantages of the larger atomic weight of Na and the lower standard electrochemical potential than that of Li in LIBs. Therefore, developing high-performance electrodes with a larger capacity, high-operation voltage, and good cycling stability is of great importance to realize the practical applications of NIBs.

Since 2010, various electrode materials have been developed for NIBs, including (1) cathodes (layered oxides,[10] polyanionic compounds,[11] Prussian blue analogs,[12] etc.) and (2) anodes[13,14] (carbon-based materials, Ti-based materials, alloy materials, chalcogen-based materials, organic materials, etc). The layered transition-metal (TM) oxides Na$_x$TMO$_2$ exhibit the potential application prospects in large-scale energy storage because of their low cost, high capacity, and flexible synthesis

The Bigger Picture

Oxygen redox activities are attracting increasing attention owing to oxygen's higher capacity for Li- and Na-ion batteries. However, the accessible structural chemistry on facilitating oxygen oxidation remains elusive for Na-deficient layered cathodes. Herein, we report that Ti substitution in Mn^{4+}-rich cathodes improves oxygen redox chemistry. The origins reveal that Ti^{4+} substitution can both decrease local ordering of transition metals and modulate electronic structure of the O 2p state. The new insights bring out more possibilities for future works.

Chem

CellPress

techniques, which can be used as both cathodes and anodes with different redox centers.[2] Common 3d TM elements used as the redox centers are Ti, V, Cr, Mn, Fe, Co, Ni, and Cu (eight species in NIBs), while several inactive elements, such as Li, Mg, Al, Zn, etc., are normally used for structure stabilization, charge balance, and electrochemical behavior improvement.[8,15–17] Therefore, understanding the structure-property chemistry of different elements used in TMO$_2$ layers will help to develop high-performance materials.

P2 and O3 structures, where P represents Na ions that are accommodated at the trigonal prismatic (P) sites and O denotes Na ions at octahedral (O) sites, are the most widely used layered materials in NIBs; the numbers 2 and 3 represent the edge-sharing TMO$_6$ octahedra with the oxygen stacking in ABBA and ABCABC modes, respectively.[18] Two-layered oxides with only Earth's abundant Ti and Mn elements, O3-Na$_{2/3}$Mg$_{1/3}$Ti$_{2/3}$O$_2$[19] and P2-Na$_{2/3}$Mg$_{1/3}$Mn$_{2/3}$O$_2$,[20] caught our attention because of their similar molecular formula but different crystal structures, where Ti^{4+} and Mn^{4+} were often used to replace each other in the same phase with a solid-solution evolution toward, for example, P2-Na$_{2/3}$Ni$_{1/3}$Ti$_{2/3}$O$_2$[21] and P2-Na$_{2/3}$Ni$_{1/3}$Mn$_{2/3}$O$_2$,[21,22] O3-NaNi$_{1/2}$Ti$_{1/2}$O$_2$,[23] and O3-NaNi$_{1/2}$Mn$_{1/2}$O$_2$.[24] Wang et al. investigated the substitution effect on P2-Na$_{2/3}$Ni$_{1/3}$Ti$_{1/3}$Mn$_{1/3}$O$_2$[25] and O3-NaNi$_{1/2}$Mn$_{3/10}$Ti$_{2/10}$O$_2$,[26,27] showing that the intermediate phase could modulate the arrangement of Na and the vacancy with a disordered distribution in NaO$_2$ layers, resulting in the high Na$^+$ mobility and the smooth charge and discharge voltage curves without multiple voltage plateaus.

Herein, in order to develop promising cathode materials, we tried to employ the chemical substitution strategy to prepare the solid-solution phases with a composition of (1 − x)O3-Na$_{2/3}$Mg$_{1/3}$Ti$_{2/3}$O$_2$-xP2-Na$_{2/3}$Mg$_{1/3}$Mn$_{2/3}$O$_2$ to study their electrochemical properties. We found that a highly pure intermediate phase of P2-Na$_{2/3}$Mg$_{1/3}$Ti$_{1/6}$Mn$_{1/2}$O$_2$ was successfully obtained when x = 3/4, as shown in Figure S1. The following investigation exhibits that the partial Ti-substituted Na$_{2/3}$Mg$_{1/3}$Ti$_{1/6}$Mn$_{1/2}$O$_2$ can result in a significant improvement in the stability of the high-voltage plateau with a total reversible capacity of ∼230 mAh g^{-1} in the voltage range of 1.5–4.5 V, where more than twice the capacity is retained in the high-voltage plateau area than in the non-Ti-substituted sample under the same cycles. This promising stabilization of the high-voltage plateau can be attributed to the decrease of the ordered Mg, Mn, and Ti distribution and the highly ionized Ti^{4+} facilitating the charge-transfer reaction.

RESULTS

Structure Characterization

Synthesis of a series of chemical substitutions of (1 − x)O3-Na$_{2/3}$Mg$_{1/3}$Ti$_{2/3}$O$_2$-xP2-Na$_{2/3}$Mg$_{1/3}$Mn$_{2/3}$O$_2$ samples was attempted by solid-state reaction at annealing temperatures from 850°C to 1,050°C at a gradient of typically 50°C and an annealing time from 6 to 24 h at a gradient of typically 6 h. With the increase of x, the amount of the O3 phase tended to decrease, but the P2 phase always played a dominant role. Unlike the continuous solid solution of (1 − x)P2-Na$_{2/3}$Ni$_{1/3}$Ti$_{2/3}$O$_2$-xP2-Na$_{2/3}$Ni$_{1/3}$Mn$_{2/3}$O$_2$ and (1 − x)O3-NaNi$_{1/2}$Ti$_{1/2}$O$_2$-xO3-NaNi$_{1/2}$Mn$_{1/2}$O$_2$ (0 ≤ x ≤ 1), (1 − x)O3-Na$_{2/3}$Mg$_{1/3}$Ti$_{2/3}$O$_2$-xP2-Na$_{2/3}$Mg$_{1/3}$Mn$_{2/3}$O$_2$ shows a phase-separation behavior, in which the P2 phase always plays the dominant role, and a small range of solid solution into the P2 type is observed with 1/2 < x ≤ 1. An optimized condition of calcination at 950°C for 24 h was found, and a highly pure P2 phase with x = 3/4 corresponding to the composition of Na$_{2/3}$Mg$_{1/3}$Ti$_{1/6}$Mn$_{1/2}$O$_2$ was successfully

^{1}Key Laboratory for Renewable Energy, Beijing Key Laboratory for New Energy Materials and Devices, Beijing National Laboratory for Condensed Matter Physics, Institute of Physics, Chinese Academy of Sciences, Beijing 100190, China

^{2}Center of Materials Science and Optoelectronics Engineering, University of Chinese Academy of Sciences, Beijing 100049, China

^{3}Department of Chemistry and Chemical Biology, Harvard University, Cambridge, MA 02138, USA

^{4}State Key Laboratory for Surface Physics, Institute of Physics, Chinese Academy of Sciences, Beijing 100190, China

^{5}Department of Chemistry and Department of Computer Science, University of Toronto, Toronto, ON M5S 3H6, Canada

^{6}Vector Institute for Artificial Intelligence, Toronto, ON M5G 1M1, Canada

^{7}Yangtze River Delta Physics Research Center Co. Ltd., Liyang 213300, China

^{8}These authors contributed equally

^{9}Lead Contact

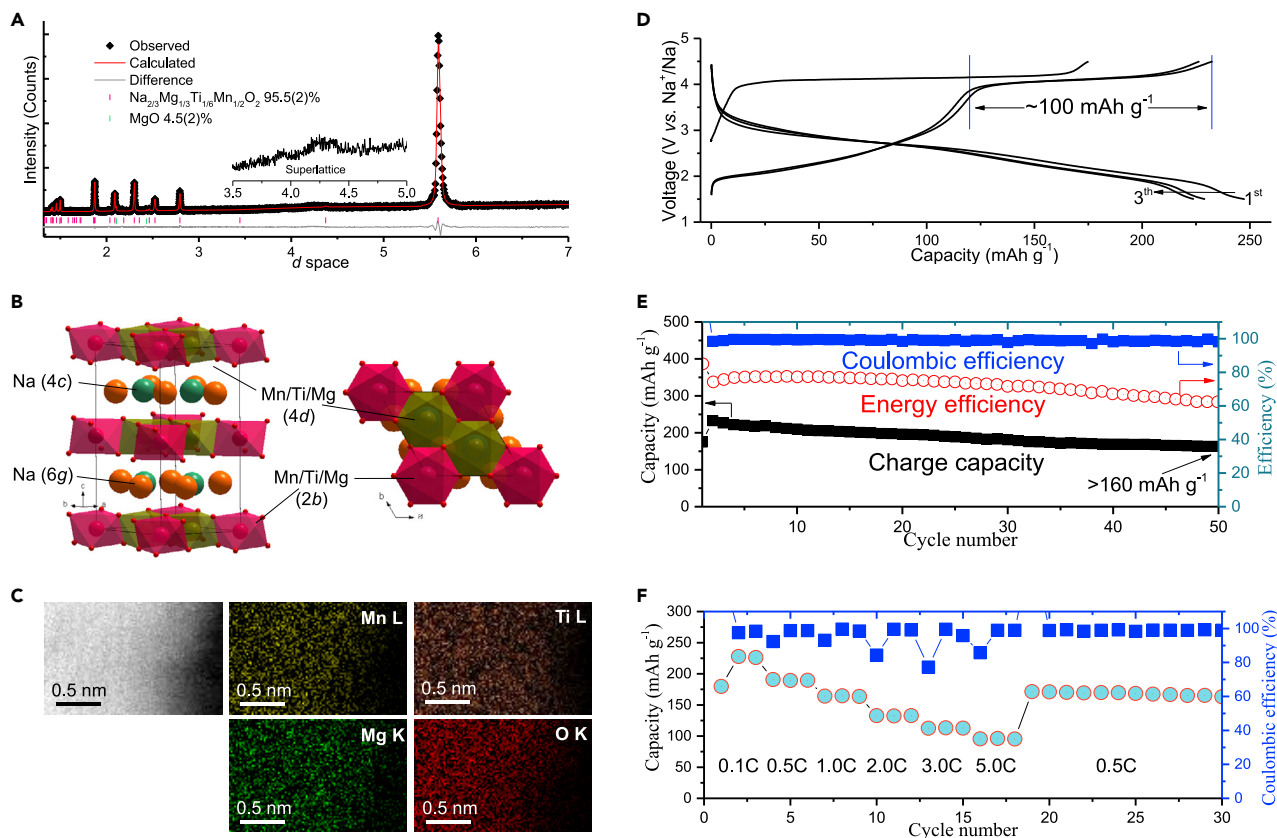*Correspondence: yxlu@iphy.ac.cn (Y.L.), aspuru@utoronto.ca (A.A.-G.), yshu@iphy.ac.cn (Y.-S.H.)

https://doi.org/10.1016/j.chempr.2019.08.003

Chem

CellPress

Figure 1. Structural Characterization of As-Prepared Na$_{2/3}$Mg$_{1/3}$Ti$_{1/6}$Mn$_{1/2}$O$_2$ and Its Electrochemical Properties in Half Cells

(A) Rietveld refinement of XRD pattern of Na$_{2/3}$Mg$_{1/3}$Ti$_{1/6}$Mn$_{1/2}$O$_2$ and the inset showing the (1/3, 1/3, l) superlattice structure of Mg and Mn(Ti) ordering.

(B) Schematic illustrations of the corresponding P2-type structure with the incomplete Mg and Mn(Ti) ordering distributed [Mg$_{1/3}$Ti$_{1/6}$Mn$_{1/2}$]O$_2$ slabs.

(C) STEM image and EELS mappings of Mn, Ti, Mg, and O elements.

(D) Charge-discharge curves cycled at a rate of 0.1 C (∼20 mA g^{-1}) in the voltage range of 1.5–4.5 V.

(E) Retention of the charge capacity, Coulombic efficiency, and energy efficiency at a rate of 0.2 C (∼40 mA g^{-1}).

(F) Rate capability of the charge capacity and Coulombic efficiency (a loading of active material ∼2 mg cm^{-2}).

obtained. High-resolution X-ray diffraction (XRD) Rietveld refinement analysis was performed to determine the crystal structure and phase purity presented in Figure 1A. About 4.5(2)% impurity phase is assigned to MgO. Combined with the inductively coupled plasma-atomic emission spectrometry (ICP-AES), the composition of the as-prepared compound is Na$_{0.674(1)}$Mg$_{0.343(1)}$Ti$_{0.169(1)}$Mn$_{0.491(1)}$O$_2$ after removing the MgO phase. The XRD pattern revealed that the partial Ti substitution in Na$_{2/3}$Mg$_{1/3}$Ti$_{1/6}$Mn$_{1/2}$O$_2$ leads to a P2-type layered structure, indexed in the hexagonal structure with the space group of $P6_3/mcm$ based on the Mg and Mn ordering structural model.[20] However, a reduced ordering of the Mg, Ti, and Mn distribution was found during the refined process, agreeing with the broad and weak (1/3, 1/3, l) superlattice peaks shown by the inset in Figure 1A. The corresponding crystallographic data, atomic coordinates, occupancies, and anisotropic displacement parameters (Å^2) are presented in Tables S1 and S2. The crystal structure of this Na$_{2/3}$Mg$_{1/3}$Ti$_{1/6}$Mn$_{1/2}$O$_2$ compound is shown in Figure 1B, where the Mg, Ti, and Mn ions are simultaneously located in two octahedral sites, 4d (1/3, 2/3, 0) and 2b (0,0,0), different from the complete Ni and Te ordering in P2-Na$_{2/3}$Ni$_{2/3}$Te$_{1/3}$O$_2$, in which Ni ions are in 4d sites and Te ions in 2b sites.[28] The morphology of this sample is characterized by scanning electron microscopy (SEM), as shown in

Chem

Figure S2; plate-like particles are exhibited with a distribution of size in the range of ~3–5 μm. The detailed crystal structure is further investigated by high-resolution transmission electron microscopy (HRTEM), where the interplanar distances between the adjacent lattice fringes are ~0.566 nm, corresponding to the d spacing value of the (002) planes of the obtained P2 phase in Figure S3. The scanning transmission electron microscopy (STEM) image and electron energy loss spectroscopy (EELS) mappings clearly revealed that Mn, Ti, Mg, and O elements are uniformly distributed in this particle.

Na-Storage Performance

The electrochemical properties were investigated in half cells with 0.2 M NaPF$_6$ and 0.8 M NaClO$_4$ in ethylene carbonate/diethyl carbonate (EC/DEC = 4:6 in volume) with fluoroethylene carbonate (FEC, 5% in volume) as the electrolyte. In Na$_{2/3}$Mg$_{1/3}$Ti$_{1/6}$Mn$_{1/2}$O$_2$, 1/2 mol Mn ions and 1/6 mol Ti ions exist in the tetravalent state of its initial design, and Mg ions are the inactive component. Therefore, the oxygen redox chemistry was expected to provide the charge compensation for Na deintercalation similar to the recently reported Mn^{4+}-based compounds, such as P2-Na$_{2/3}$Mg$_{0.28}$Mn$_{0.72}$O$_2$,[29,30] P2- and P3-Na$_{2/3}$Mg$_{1/3}$Mn$_{2/3}$O$_2$,[31,32] etc. To the best of our knowledge, there is no previous work exploring the influence of chemical substitution of Ti to Mn on chemical and electrochemical properties of this kind of cathode material in NIBs. Understanding the structure-property relationship of the Ti substitution may be helpful to develop high-performance cathode materials for the low-cost NIBs, where both the Mn and Ti are the Earth's abundant TM elements. When cycled in the voltage range from 1.5 to 4.5 V, a higher reversible capacity of ~230 mAh g^{-1} is achieved in Figure 1D, and a well-defined voltage plateau is observed at ~4.1 V in the initial charge process. During the following cycles, this high-voltage plateau is still obviously presented with a large capacity of ~100 mAh g^{-1}. Compared to non-Ti-substituted Mg^{2+}- and Mn^{4+}-based cathodes of P2-Na$_{2/3}$Mg$_y$Mn$_{1-y}$O$_2$,[29,31,32] the obtained P2-Na$_{2/3}$Mg$_{1/3}$Ti$_{1/6}$Mn$_{1/2}$O$_2$ shows a higher initial charge and discharge capacity and a smaller voltage hysteresis as shown in Figure S4, demonstrating that the voltage of the redox process can be adjusted in the same crystal structure with a similar composition. About 0.1 V voltage drop is found in Figure S5. A quasi open circuit voltage (QOCV) test of this sample is displayed in Figure S6, which indicates that the equilibrium potential is achieved at ~3.94 V compared to the 4.07 V in non-Ti-substituted Na$_{2/3}$Mg$_{1/3}$Mn$_{2/3}$O$_2$.[32] Moreover, after 50 cycles, a capacity of >160 mAh g^{-1} is retained, higher than that of the non-Ti-substituted cathodes in Figures 1E and S4. In addition, an enhanced rate capability is also exhibited in Figure 1F, where ~100 mAh g^{-1} is retained at a rate of 5 C corresponding to 500 mA g^{-1} with ~2 mg cm^{-2} loading of the active material.

Figures S7 and S8 present the charge-discharge curves at different cycles, in which the high-voltage plateau shows good stability. About 50 mAh g^{-1} capacity from this high-voltage plateau area is retained after 50 cycles. The dQ/dV plots in Figure S9 show that the total capacities come from the Mn^{3+}/Mn^{4+} and O^{2-}/O$^-$ redox couples.[32] This high-voltage plateau is critical for the high energy density of a battery. Compared to the non-Ti-substituted materials, the high-voltage plateau of Ti-substituted material shows more superior behaviors in the stability. The comparison of charge curves of the Mn/Mg-based P2-Na$_{2/3}$Mg$_{0.28}$Mn$_{0.72}$O$_2$,[29] P2-Na$_{2/3}$Mg$_{1/3}$Mn$_{2/3}$O$_2$,[32] and P3-Na$_{2/3}$Mg$_{1/3}$Mn$_{2/3}$O$_2$[31] with this as-prepared P2-Na$_{2/3}$Mg$_{1/3}$Ti$_{1/6}$Mn$_{1/2}$O$_2$ is shown in Figures 2A–2E with the 1st, 5th, 10th, 30th, and 50th cycles. The P2-Na$_{2/3}$Mg$_{1/3}$Mn$_{2/3}$O$_2$ and P3-Na$_{2/3}$Mg$_{1/3}$Mn$_{2/3}$O$_2$ deliver the larger initial charge capacity but with a fast decrease in the following cycles. More than twice the capacity is preserved in this high-voltage plateau area of
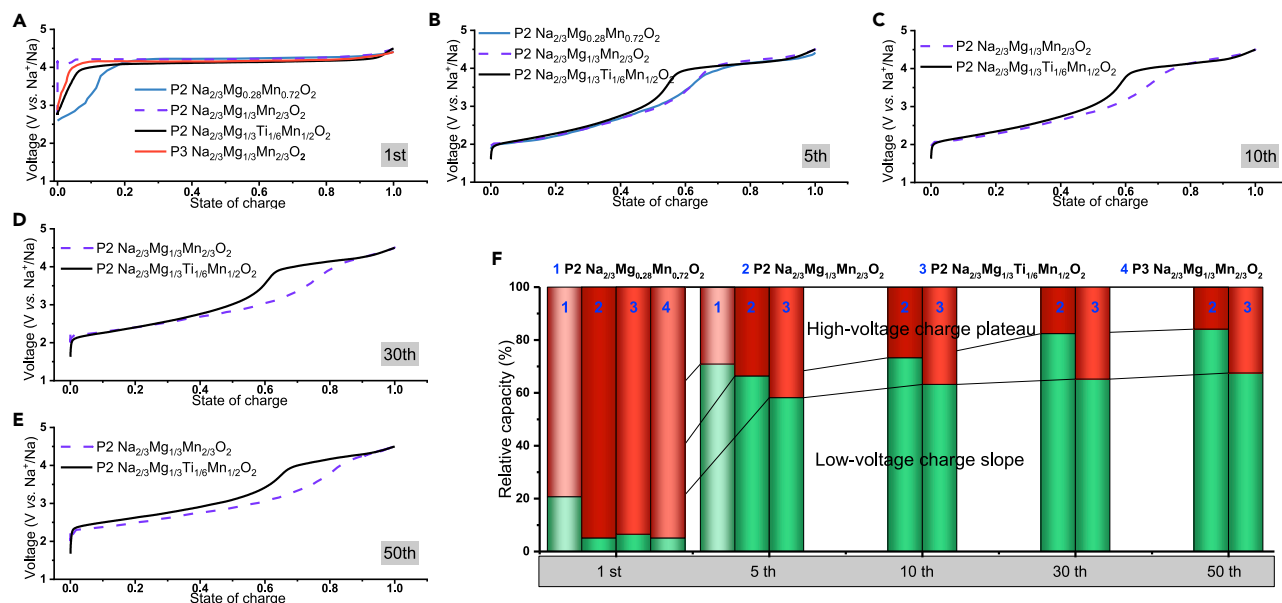
Figure 2. Comparison of Charge Curves of the Mn- and Mg-Based P2-Na$_{2/3}$Mg$_{0.28}$Mn$_{0.72}$O$_2$, P2-Na$_{2/3}$Mg$_{1/3}$Mn$_{2/3}$O$_2$, and P3-Na$_{2/3}$Mg$_{1/3}$Mn$_{2/3}$O$_2$ and the As-Prepared P2-Na$_{2/3}$Mg$_{1/3}$Ti$_{1/6}$Mn$_{1/2}$O$_2$ at Different Cycles

(A–E) The 1st (A), 5th (B), 10th (C), 30th (D), and 50th (E) cycles.

(F) Relative capacity of the Ti-substituted P2-Na$_{2/3}$Mg$_{1/3}$Ti$_{1/6}$Mn$_{1/2}$O$_2$ versus the other Mn- and Mg-based cathodes at different cycles; the red area represents the high-voltage plateau capacity and the green is the low-voltage slope capacity.

the as-prepared Na$_{2/3}$Mg$_{1/3}$Ti$_{1/6}$Mn$_{1/2}$O$_2$ against the P2-Na$_{2/3}$Mg$_{1/3}$Mn$_{2/3}$O$_2$ cathode after 50 cycles. The relative capacities from the high-voltage plateau region and the low-voltage slope part are showed in Figure 2F, which demonstrates that Na$_{2/3}$Mg$_{1/3}$Ti$_{1/6}$Mn$_{1/2}$O$_2$ exhibits a larger high-voltage plateau capacity after the initial charge with a slow decay trend.

Insights into the Structural Evolution

In order to obtain more insights of the structural evolution during the Na (de)intercalation process and the specific influence of Ti substitution on the host lattice, *in situ* XRD data are collected in the charge-discharge process in the voltage range of 1.5–4.5 V at a rate of 0.08 C, where four states with the pristine, fully charged at 4.5 V, fully discharged at 1.5 V, and then secondly charged to 4.1 V are highlighted with purple, orange, blue, and red colors, respectively, in Figure 3A. Combined with Figure 3B, this material experiences a phase transition from the P2 structure to the O2 structure upon ~0.40 mol Na$^+$ deintercalation with a typical (002) peak being presented at about 18°. This P2-O2 transition is usually observed in the P2-type cathodes along with the O2 peaks becoming much stronger and the original P2 peaks much weaker with further Na$^+$ deintercalation.[15,29] However, the newly formed O2 phase of this compound does not become more intense even at ~0.6 mol Na$^+$ deintercalation from the pristine structure, and a large ratio of (002) peaks for P2 and O2 is found upon deep charging to 4.5 V in Figure 3C, which differs from the non-Ti-substituted Na$_{2/3}$Mg$_{0.28}$Mn$_{0.72}$O$_2$.[29] The O2 phase shows significantly broadened (002) diffraction lines when charged to 4.5 V, which suggests some located stacking faults occurred due to the two different gliding vectors of the P2-O2 phase transition.[20] However, during the first discharge process, this phase transition is observed to be a reversible process, and the O2 phase diffraction lines disappear with further Na$^+$ intercalation. After discharging below ~2.2 V, a monoclinic P'2 phase begins to
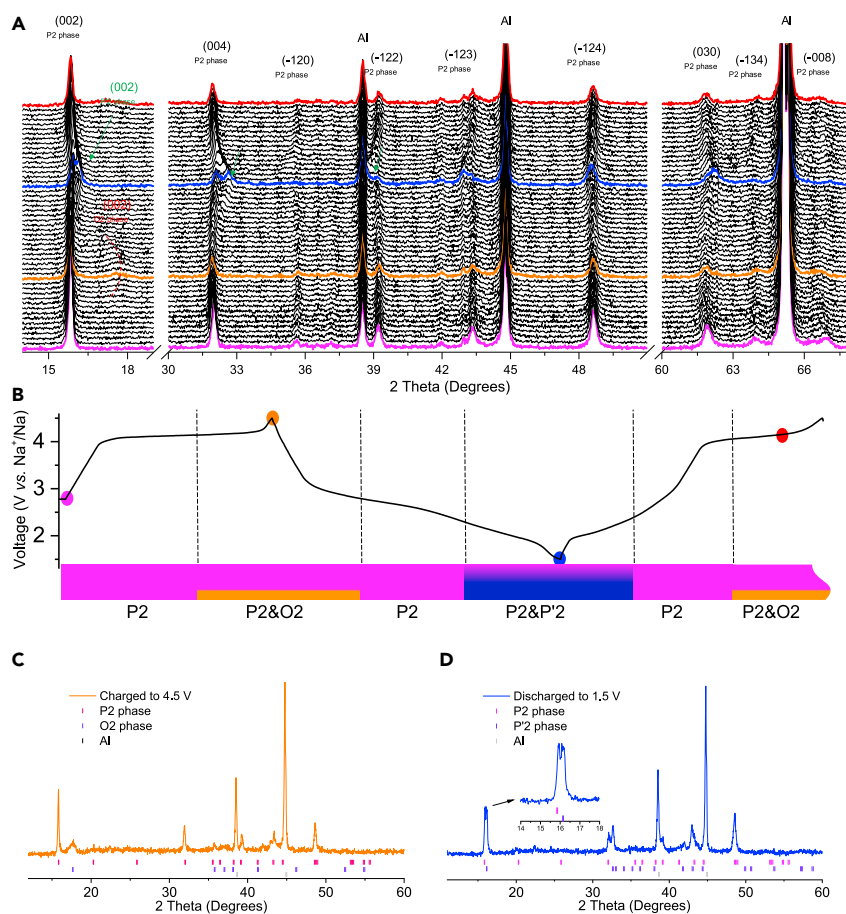
Chem

CellPress

Figure 3. Structural Evolution of Na$_{2/3}$Mg$_{1/3}$Ti$_{1/6}$Mn$_{1/2}$O$_2$ during the Charge-Discharge Process in the Voltage Range of 1.5–4.5 V

(A) *In situ* XRD patterns collected at a rate of 0.08 C and four states with the pristine, fully charged at 4.5 V, fully discharged at 1.5 V, and then secondly charged to 4.1 V are highlighted with purple, orange, blue, and red colors, respectively.

(B) Correlation of the electrochemical curve of the phase composition range determined from *in situ* XRD, and monophasic and/or biphasic domains are stated, respectively.

(C) The fully charged state XRD pattern containing a dominant P2 phase and small amount of O2 phase with the broadened (002) peak.

(D) The fully discharged state XRD pattern containing biphasic domains with the P2 phase and a new formed P'2 phase and the P'2 phase indexed in monoclinic space group.

form, which is similar to the P2-type Mn-based cathodes,[33] and upon discharge to 1.5 V more Mn^{3+} is produced with relation to the larger amount of the P'2 phase as shown in Figure 3D. All the phase transitions are reversible, and they would be back in the following Na (de)intercalation (Figure S10). The superstructure peaks at 19°–22° of the as-prepared cathode are shown in Figure S11; no obvious changes demonstrate that the in-plane cation distribution is not influenced by Na (de)intercalation in the charge-discharge process, where the weak peaks can be related to the reduced ordering of Mg, Ti, and Mn ions. After one cycle, this layered P2 structure is found to be recovered with the presence of much sharper peaks against the non-Ti-substituted materials, and no irreversible transition of lattice oxygen stacking sequences is observed, unlike the P3-Na$_{2/3}$Mg$_{1/3}$Mn$_{2/3}$O$_2$ cathode with a P3 to O3 phase transition.[31]

Chem

CellPress

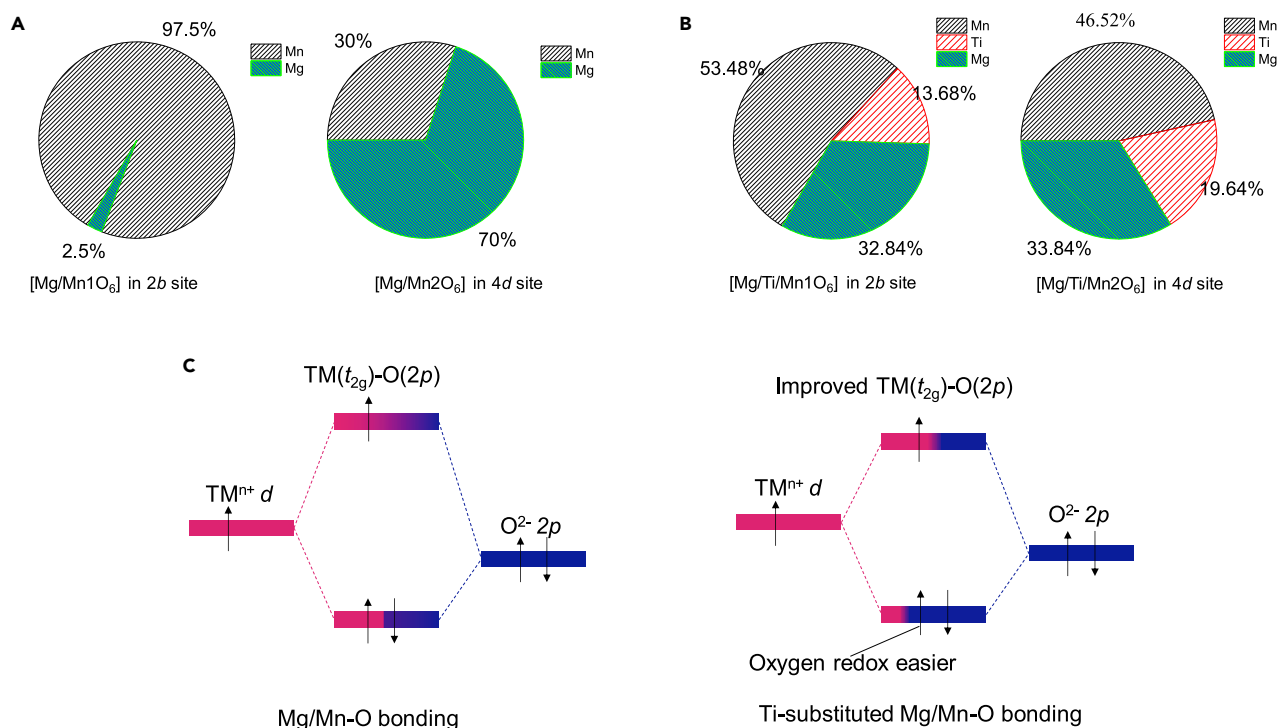**Figure 4. Stabilization Mechanisms of High-Voltage Plateau in the Ti-Substituted P2-$Na_{2/3}Mg_{1/3}Ti_{1/6}Mn_{1/2}O_2$ Cathode**

(A and B) Proportion of TM elements in different occupancies of the (A) non-Ti-substituted and (B) Ti-substituted compounds from the Rietveld refinement results. Ti substitution makes the elements distribution more disordering compared to the non-Ti substitution.

(C) Schematic illustration of the electron energy level diagram showing the TM(t_{2g})-O($2p$) and improved TM(t_{2g})-O($2p$) bonding interactions in non-Ti-substituted Mn– and Mg–O bonding and Ti-substituted Mg–, Ti–, and Mn–O bonding. The different colors represent the contribution from TMs and oxygen redox, respectively.

DISCUSSION

Different from the continuous solid solution of $(1 − x)$P2-$Na_{2/3}Ni_{1/3}Ti_{2/3}O_2$-$x$P2-$Na_{2/3}Ni_{1/3}Mn_{2/3}O_2$ and $(1 − x)$O3-$NaNi_{1/2}Ti_{1/2}O_2$-xO3-$NaNi_{1/2}Mn_{1/2}O_2$ $(0 \leq x \leq 1)$, $(1 − x)$O3-$Na_{2/3}Mg_{1/3}Ti_{2/3}O_2$-$x$P2-$Na_{2/3}Mg_{1/3}Mn_{2/3}O_2$ shows a phase-separation behavior, in which the P2 phase always plays the dominant role and a small range of solid solution into the P2 type is observed with $1/2 < x \leq 1$. The obtained P2-$Na_{2/3}Mg_{1/3}Ti_{1/3}Mn_{1/2}O_2$ exhibits a significant improved stability on the high-voltage plateau with enhanced total reversible capacity of $\sim$230 mAh g^{-1}, which is critical for the high energy density of NIBs. Understanding the structure-property relationship of the Ti substitution would undoubtedly be vital to develop high-performance cathode materials. In this work, Ti^{4+} substitution to Mn^{4+} in the P2-$Na_{2/3}Mg_{1/3}Mn_{2/3}O_2$ host leads to the difference on both the pristine crystal structure and the electron distribution, which can be related to the improved electrochemical properties. The Mg and Mn ordering in the TMO_2 layers has generally been observed in the $Na_{2/3}Mn_xMg_{1-x}O_2$ because of the big difference of the ionic radius (Mg^{2+}:$R_{CN=6}$ = 0.72 Å, Mn^{4+}:$R_{CN=6}$ = 0.53 Å),[34] similar to P2-$Na_{2/3}Mg_{1/3}Mn_{2/3}O_2$ with $(1/3, 1/3, l)$ superlattice peaks. However, in the O3-type $Na_{2/3}Mg_{1/3}Ti_{2/3}O_2$ compound, Mg and Ti ions are distributed in a disordered state, corresponding to the small difference on the ionic radius (Mg^{2+}:$R_{CN=6}$ = 0.72 Å, Ti^{4+}:$R_{CN=6}$ = 0.605 Å).[34] The occupancies of TM sites for the non-Ti-substituted and Ti-substituted compounds are shown in Figure 4A obtained from the Rietveld refinement results. For the non-Ti-substituted compound, the obvious preference of Mn^{4+} in the $4d$ site and Mg^{2+} in $2b$ site are observed in Table S3, which can be indicated by the

intense superlattice peaks.[20] The Ti-substituted Na$_{2/3}$Mg$_{1/3}$Ti$_{1/3}$Mn$_{1/2}$O$_2$ compound gives the unobvious preference of the Mg^{2+} and Mn^{4+} distribution, which can be attributed to the Ti^{4+} introduction that mitigates the radius differences among ions in TMO$_2$ slabs. The weak ordered peaks have been observed in the XRD pattern, as shown in Figure S11. In the case of the Li$_2$MnO$_3$-based cathodes in LIBs, a potential cation rearrangement often appears in the host structure upon charging to the high-voltage plateau (~4.5 V), and the Li and TM ordering will decrease after the initial charge.[35,36] These similar behaviors have also been observed in non-Ti-substituted Na$_{2/3}$Mg$_{0.28}$Mn$_{0.72}$O$_2$,[29,30] where the superlattice lines at ~21.5° are found to weaken gradually during the charge process, and these weakened superlattice lines are not even recovered at the end of discharge. This indicates the in-plane cation ordering has been affected after oxygen redox or cation rearrangements. However, in this Ti-substituted Na$_{2/3}$Ni$_{1/3}$Ti$_{1/3}$Mn$_{1/3}$O$_2$ compound, the weak Mg, Mn, and Ti ordering is not influenced after charging to the high-voltage plateau. This phenomenon has also been demonstrated by Ti-substituted P2-Na$_{2/3}$Ni$_{1/3}$Mn$_{1/3}$Ti$_{1/3}$O$_2$[25] and Na$_{0.6}$Cr$_{0.6}$Ti$_{0.4}$O$_2$,[37] in which Ti substitution can diminish TM ordering distribution, leading to a highly reversible structural evolution. The pristine Ti-substituted P2 Na$_{2/3}$Mg$_{1/3}$Ti$_{1/6}$Mn$_{1/2}$O$_2$ oxide presents a smaller interlayer distance ($d_{\text{O-Na-O}}$) of 3.6707 Å than that of 3.8003 Å in non-Ti-substituted oxides.[20,29] $d_{\text{O-Na-O}}$ is the perpendicular interlayer distance between the two oxygen layers enclosing the Na ions. The phase transition from P type to O type can be attributed to the slide of the TMO$_2$ slabs on the deep extraction of Na$^+$, where the flexibility of the phase transition process is related to the relative interlayer space. This smaller distance can increase the difficulty of sliding, suppressing the further phase transition.

Furthermore, Ti^{4+} in the d^0 configuration has no valence electron, leading to significantly lower redox possibility upon charging. Compared to Mn–O bonding, electrons are more localized around O ions in Ti-O bonding, which can be beneficial to facilitate the oxidation of oxygen ions,[38–40] as illustrated in Figure 4B. As a result, more than two-times capacity from this high-voltage plateau is presented for the Ti-substituted cathode than that of the non-Ti-substituted cathode under the same cycles. First-principles density functional theory (DFT) calculations have been widely used as effective tools to study battery materials via determining electronic structures of electrode materials.[37–39] Therefore, we tried to identify the structures of Na$_{2/3}$Mg$_{1/3}$Mn$_{2/3}$O$_2$ and Na$_{2/3}$Mg$_{1/3}$Ti$_{1/6}$Mn$_{1/2}$O$_2$ based on the ground-state phase determination method as shown in Figure 5. For the Ti-substituted system, the lower-lying Ti 3d t_{2g} level confirms the low redox possibility of Ti^{4+} and electron localization around O ions. These electrons will then further boost the O 2p levels as shown in Figure 5. Considering the smaller stochiometric amount of Ti (1/6) compared to Mn (1/2), many oxygen ions in the Ti-O bonding are also in the Mn–O bonding. Therefore, the Mn 3d t_{2g} level will experience a concomitant elevation as a result of the larger number of electrons on the hybrid Mn–O orbital. The elevated O 2p level makes the oxygen redox more accessible, which will eventually occur at a relatively lower charge voltage because of its closer distance to the Fermi level, validating the observed charge voltage decrement (~0.1 V) compared to the non-Ti substitution system. Therefore, the introduction of Ti^{4+} facilitates oxygen oxidation with an enhanced reversible capacity in the Na$_{2/3}$Mg$_{1/3}$Ti$_{1/6}$Mn$_{1/2}$O$_2$ cathode. Owing to a similar electronic configuration, Nb^{5+}(d^0) shows similar ionized property to Ti^{4+}(d^0), which has been observed with the similar behaviors in cation-disordered Li$_{1.3}$Nb$_{0.3}$Mn$_{0.4}$O$_2$.[41] However, the larger atomic weight and the structural incompatibility (Nb^{5+} does not prefer to form a layered oxide) should be taken into consideration. Nevertheless, there is a concern that this cathode material is not suitable to be paired with
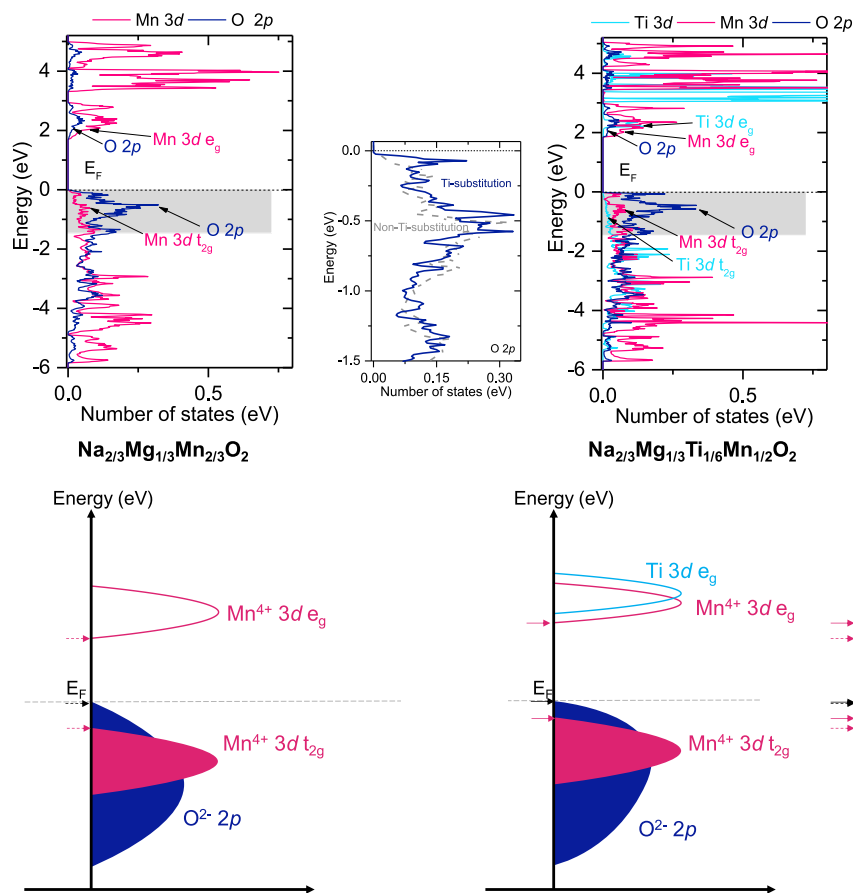
Chem

CellPress

Figure 5. Electronic Structure Evolution Partial Density of States and the Schematic Illustration of the Energy versus DOS with the Corresponding Voltage

The pDOS O 2p and Mn 3d states are represented in light purple and blue, respectively. The Fermi energy is set to 0 eV.

non-Na-containing anode materials (e.g., hard carbon anodes) to fabricate full cells, in which the pre-sodiation strategy is necessary.

In summary, a new cathode of $Na_{2/3}Mg_{1/3}Ti_{1/6}Mn_{1/2}O_2$ has been successfully prepared based on the chemical substitution between O3-$Na_{2/3}Mg_{1/3}Ti_{2/3}O_2$ and P2-$Na_{2/3}Mg_{1/3}Mn_{2/3}O_2$. It exhibits a highly reversible capacity of ~230 mAh g^{-1} with a highly stable high-voltage plateau at ~4.1 V. This work demonstrates that Ti substitution can reduce the Mg and Mn ordering in TMO$_2$ layers and facilitate oxygen oxidation with an enhanced reversible performance.

EXPERIMENTAL PROCEDURES

Sample Synthesis

The resulting material of $Na_{2/3}Mg_{1/3}Ti_{1/6}Mn_{1/2}O_2$ was prepared by a solid-state reaction. The stoichiometric precursors of NaNO$_3$ (>98%), MgO (>97%), MnO$_2$ (99%), and TiO$_2$ (99.5%, anatase) were thoroughly mixed in an agate mortar and pressed into pellets under a pressure of 10 MPa, which was further calcined at 950°C for 24 h with intermediate grinding and cooled to room temperature naturally. After the heat treatment, the material was directly put into an Ar-filled glovebox to prevent any moisture exposure.

Chem

Material Characterizations

Powder XRD was performed using a Bruker D8 Advance diffractometer equipped with a Cu Kα radiation source (λ_1 = 1.54060 and λ_2 = 1.54439 Å) and a LynxEye_XE detector. Rietveld refinement of the XRD was carried out using the general structure analysis system (GSAS) software with the EXPGUI software interface.[42] The morphologies and sizes of these materials were observed with a scanning electron microscope (Hitachi S-4800). HR-TEM images, STEM images, and EELS mappings were obtained using a 300 kV aberration-corrected (S)TEM (JEM-ARM300F, JEOL Ltd.) operated at 300 kV with a cold field emission gun and double dodecapoles Cs correctors. The stoichiometry of the as-synthesized compound was determined and measured by ICP-AES. In *in situ* XRD studies, the working electrode was prepared using polyvinylidene fluoride (PVDF) as the binder on an Al foil. A specially designed Swagelok cell equipped with an X-ray transparent Al window was used for the measurements cycled at a current rate of 0.08 C in the voltage range of 1.5–4.5 V.

Electrochemical Measurement

The working electrodes were prepared via mixing 80 wt % active material with 12 wt % acetylene black and 8 wt % PVDF on Al foil where the loading mass of the active material was ~5 mg cm^{-2}. The prepared electrodes were dried at 100°C under vacuum for 12 h and then were fabricated into CR2032 coin-type cells with pure sodium foil as the counter electrode in an argon-filled glove box (H$_2$O, O$_2$ < 0.1 ppm). A glass fiber was used as the separator, and 0.2 M NaPF$_6$ and 0.8 M NaClO$_4$ in EC/DEC (EC/DEC = 4:6 in volume) with FEC (5% in volume) was used as the electrolyte. The charge and discharge measurements were carried out on a Land BT2000 battery test system (Wuhan, China) in voltage range of 1.5–4.5 V under room temperature. Galvanostatic intermittent titration technique (GITT) was measured with Maccor instrument by applying the repeated current pulses for 30 min at a current density of 20 mA g^{-1} followed by relaxation for 10 h. The relaxation time was set longer in order to achieve the equilibrium potential for the given electrode.

Computational Methods

All first-principle DFT calculations reported in this study were performed using the Vienna *Ab Initio* Simulation Package (VASP)[43–46] with the projector augmented wave (PAW) potentials[47] and the Perdew-Becke-Ernzerhof (PBE)[48] exchange correlation. A plane-wave basis with a cutoff energy of 520 eV and Γ-centered k-meshes with a density of 8,000 k-points per reciprocal atom were used for all calculations. All calculations were spin polarized, with Mn atoms initialized in a high-spin configuration and relaxed to self-consistency with the ferromagnetic (FM) configurations applied. The DFT + U method introduced by Dudarev et al.[49] was used to treat the localized 3d electrons of Mn with a U of 3.8, obtained by fitting it to experimental and calculated formation enthalpies in a previous study.[50] The lowest-energy, ground-state structure of Na$_{2/3}$Mg$_{1/3}$Mn$_{2/3}$O$_2$ and Na$_{2/3}$Mg$_{1/3}$Ti$_{1/6}$Mn$_{1/2}$O$_2$ are determined by a vast number of geometrically distinct Na-vacancy and Mg-Na-Mn ordered configurations using the DFT-calculation-based NEPS method.[51,52] Starting from the partially occupied structure from the XRD refinement, which has Na and a vacancy sharing the Na sites and Mg and Mn (Ti) sharing the metal sites as shown in Figure S13, we generate supercells containing 12 Na sites and 12 metal sites. We then populate the metal sites with Mg and Mn in the ratio 1:2 and introduce vacancies (vacancy on the Na sites with a Na/vacancy ratio of 2:1). 3,150 geometrically different configurations were generated using the Enum code.[53–55] We calculated the electrostatic total energy for all configurations using nominal charge states for the ions in the system as a quick energy sampling step.[56] All structures were ranked by their normalized electrostatic energies, and the 100 Na$_{2/3}$Mg$_{1/3}$Mn$_{2/3}$O$_2$

Chem

CellPress

structures with the lowest electrostatic energies were fully relaxed and their energies were calculated using DFT. We find the structure with the lowest DFT total energy, i.e., the ground-state structure of Na$_{2/3}$Mg$_{1/3}$Mn$_{2/3}$O$_2$, has a space group of *Cmcm*. The ground-state structure of Na$_{2/3}$Mg$_{1/3}$Ti$_{1/6}$Mn$_{1/2}$O$_2$ is then determined by replacing 1/4 of the Mn ions in the Na$_{2/3}$Mg$_{1/3}$Mn$_{2/3}$O$_2$ structure, the total energies of all geometrically distinct structures are calculated using DFT, and the configuration with the lowest DFT total energy is selected.

SUPPLEMENTAL INFORMATION

Supplemental Information can be found online at https://doi.org/10.1016/j.chempr. 2019.08.003.

AUTHOR CONTRIBUTIONS

Y.-S.H. and Y.L. provided the direction and advice for the study. C.Z. performed the synthesis procedures, experimental investigation, and software programing to process and present collected data; Z.Y. and A.A.-G. conceived the DFT calculations of the ground-state structure prediction, electronic structure analysis, and so on; J.W. and X.B. performed the TEM observation and analysis with C.Z. C.Z., Z.Y., Y.L., and Y.-S.H. wrote the manuscript. All authors participated in the discussion to improve the manuscript. C.Z. and Z.Y. contributed equally to this work.

DECLARATION OF INTERESTS

The authors declare no competing interests.

REFERENCES AND NOTES

1. Palomares, V., Serras, P., Villaluenga, I., Hueso, K.B., Carretero-González, J., and Rojo, T. (2012). Na-ion batteries, recent advances and present challenges to become low cost energy storage systems. Energy Environ. Sci. 5, 5884–5901.

2. Li, Y., Lu, Y., Zhao, C., Hu, Y.-S., Titirici, M.-M., Li, H., Huang, X., and Chen, L. (2017). Recent advances of electrode materials for low-cost sodium-ion batteries towards practical application for grid energy storage. Energy Storage Mater. 7, 130–151.

3. Nayak, P.K., Yang, L., Brehm, W., and Adelhelm, P. (2018). From lithium-ion to sodium-ion batteries: advantages, challenges, and surprises. Angew. Chem. Int. Ed. 57, 102–120.

4. Zhao, C., Lu, Y., Chen, L., and Hu, Y.-S. (2019). Ni-based cathode materials for Na-ion batteries. Nano Res. https://doi.org/10.1007/s12274-019-2451-3.

5. Zhao, C., Liu, L., Qi, X., Lu, Y., Wu, F., Zhao, J., Yu, Y., Hu, Y.-S., and Chen, L. (2018). Solid-state sodium batteries. Adv. Energy Mater. 8, 1703012.

6. Luo, W., Shen, F., Bommier, C., Zhu, H., Ji, X., and Hu, L. (2016). Na-Ion battery anodes: materials and electrochemistry. Acc. Chem. Res. 49, 231–240.

7. Hwang, J.Y., Myung, S.T., and Sun, Y.K. (2017). Sodium-ion batteries: present and future. Chem. Soc. Rev. 46, 3529–3614.

8. Mu, L., Xu, S., Li, Y., Hu, Y.S., Li, H., Chen, L., and Huang, X. (2015). Prototype sodium-ion batteries using an Air-Stable and Co/Ni-Free O3-layered metal oxide cathode. Adv. Mater. 27, 6928–6933.

9. Wang, Q.C., Meng, J.K., Yue, X.Y., Qiu, Q.Q., Song, Y., Wu, X.J., Fu, Z.W., Xia, Y.Y., Shadike, Z., Wu, J., et al. (2019). Tuning P2-structured

cathode material by Na-site Mg substitution for Na-Ion batteries. J. Am. Chem. Soc. 141, 840–848.

10. Yao, H.R., Wang, P.F., Gong, Y., Zhang, J., Yu, X., Gu, L., OuYang, C., Yin, Y.X., Hu, E., Yang, X.Q., et al. (2017). Designing air-stable O3-type cathode materials by combined structure modulation for Na-Ion batteries. J. Am. Chem. Soc. 139, 8440–8443.

11. Gao, H., Seymour, I.D., Xin, S., Xue, L., Henkelman, G., and Goodenough, J.B. (2018). Na$_3$MnZr(PO$_4$)$_3$: a high-voltage cathode for sodium batteries. J. Am. Chem. Soc. 140, 18192–18199.

12. Song, J., Wang, L., Lu, Y., Liu, J., Guo, B., Xiao, P., Lee, J.J., Yang, X.Q., Henkelman, G., and Goodenough, J.B. (2015). Removal of interstitial H$_2$O in hexacyanometallates for a superior cathode of a sodium-ion battery. J. Am. Chem. Soc. 137, 2658–2664.

13. Zhao, C., Wang, Q., Lu, Y., Li, B., Chen, L., and Hu, Y.-S. (2018). High-temperature treatment induced carbon anode with ultrahigh Na storage capacity at low-voltage plateau. Sci. Bull. 63, 1125–1129.

14. Lu, Y., Zhao, C., Qi, X., Qi, Y., Li, H., Huang, X., Chen, L., and Hu, Y.-S. (2018). Pre-oxidation-tuned microstructures of carbon anodes derived from pitch for enhancing Na storage performance. Adv. Energy Mater. 8, 1800108.

15. Wang, P.F., You, Y., Yin, Y.X., Wang, Y.S., Wan, L.J., Gu, L., and Guo, Y.G. (2016). Suppressing the P2–O2 phase transition of Na$_{0.67}$Mn$_{0.67}$Ni$_{0.33}$O$_2$ by magnesium substitution for improved sodium-ion batteries. Angew. Chem. Int. Ed. 55, 7445–7449.

16. Wang, P.-F., You, Y., Yin, Y.-X., and Guo, Y.-G. (2018). Layered oxide cathodes for sodium-ion batteries: phase transition, air stability, and performance. Adv. Energy Mater. 8, 1701912.

17. Wang, H., Liao, X.-Z., Yang, Y., Yan, X., He, Y.-S., and Ma, Z.F. (2016). Large-scale synthesis of NaNi$_{1/3}$Fe$_{1/3}$Mn$_{1/3}$O$_2$ as high performance cathode materials for sodium ion batteries. J. Electrochem. Soc. 163, 565–A570.

18. Delmas, C., Fouassier, C., and Hagenmuller, P. (1980). Structural classification and properties of the layered oxides. Physica B+C 99, 81–85.

19. Zhao, C., Avdeev, M., Chen, L., and Hu, Y.S. (2018). An O3-type oxide with low sodium content as the phase-transition-free anode for sodium-ion batteries. Angew. Chem. Int. Ed. 57, 7056–7060.

20. Paulsen, J.M., Donaberger, R.A., and Dahn, J.R. (2000). Layered T2-, O6-, O2-, and P2-type A$_{2/3}$[M'$^{2+}_{1/3}$M$^{4+}_{2/3}$]O$_2$ bronzes, A = Li, Na. Chem. Mater. 12, 2257–2267.

21. Shanmugam, R., and Lai, W. (2014). Na$_2$Ni$_{1/3}$Ti$_{2/3}$O$_2$: "bi-functional" electrode materials for Na-Ion batteries. ECS Electrochem. Lett. 3, A23–A25.

22. Shanmugam, R., and Lai, W. (2015). Study of transport properties and interfacial kinetics of Na$_{2/3}$[Ni$_{1/3}$Mn$_x$Ti$_{2/3-x}$]O$_2$(x = 0,1/3) as electrodes for Na-Ion batteries. J. Electrochem. Soc. 162, A8–A14.

23. Yu, H., Guo, S., Zhu, Y., Ishida, M., and Zhou, H. (2014). Novel titanium-based O3-type NaTi$_{0.5}$Ni$_{0.5}$O$_2$ as a cathode material for sodium ion batteries. Chem. Commun. (Camb.) 50, 457–459.

24. Komaba, S., Yabuuchi, N., Nakayama, T., Ogata, A., Ishikawa, T., and Nakai, I. (2012). Study on the reversible electrode reaction of Na$_{1-x}$Ni$_{0.5}$Mn$_{0.5}$O$_2$ for a rechargeable sodium-ion battery. Inorg. Chem. 51, 6211–6220.

25. Wang, P.F., Yao, H.R., Liu, X.Y., Yin, Y.X., Zhang, J.N., Wen, Y., Yu, X., Gu, L., and Guo, Y.G. (2018). Na$^+$/vacancy disordering promises high-rate Na-ion batteries. Sci. Adv. 4, eaar6018.

26. Wang, H., Xiao, Y., Sun, C., Lai, C., and Ai, X. (2015). A type of sodium-ion full-cell with a layered NaNi$_{0.5}$Ti$_{0.5}$O$_2$ cathode and a pre-sodiated hard carbon anode. RSC Adv. 5, 106519–106522.

27. Wang, P.F., Yao, H.R., Liu, X.Y., Zhang, J.N., Gu, L., Yu, X.Q., Yin, Y.X., and Guo, Y.G. (2017). Ti-substituted NaNi$_{0.5}$Mn$_{0.5-x}$Ti$_x$O$_2$ cathodes with reversible O3–P3 phase transition for high-performance sodium-ion batteries. Adv. Mater. 29, 28295700.

28. Nalbandyan, V.B., Petrenko, A.A., and Evstigneeva, M.A. (2013). Heterovalent substitutions in Na2M2TeO6 family: crystal structure, fast sodium ion conduction and phase transition of Na2LiFeTeO6. Solid State Ion. 233, 7–11.

29. Yabuuchi, N., Hara, R., Kubota, K., Paulsen, J., Kumakura, S., and Komaba, S. (2014). A new electrode material for rechargeable sodium batteries: P2-type Na$_{2/3}$[Mg$_{0.28}$Mn$_{0.72}$]O$_2$ with anomalously high reversible capacity. J. Mater. Chem. A 2, 16851–16855.

30. Maitra, U., House, R.A., Somerville, J.W., Tapia-Ruiz, N., Lozano, J.G., Guerrini, N., Hao, R., Luo, K., Jin, L., Pérez-Osorio, M.A., et al. (2018). Oxygen redox chemistry without excess alkali-metal ions in Na$_{2/3}$[Mg$_{0.28}$Mn$_{0.72}$]O$_2$. Nat. Chem. 10, 288–295.

31. Song, B., Hu, E., Liu, J., Zhang, Y., Yang, X.-Q., Nanda, J., Huq, A., and Page, K. (2019). A novel P3-type Na$_{2/3}$Mg$_{1/3}$Mn$_{2/3}$O$_2$ as high capacity sodium-ion cathode using reversible oxygen redox. J. Mater. Chem. A 7, 1491–1498.

32. Dai, K., Wu, J., Zhuo, Z., Li, Q., Sallis, S., Mao, J., Ai, G., Sun, C., Li, Z., Gent, W.E., et al. (2018). High reversibility of lattice oxygen redox quantified by direct bulk probes of both anionic and cationic redox reactions. Joule 2, 518–541.

33. Wang, Q., Yang, W., Kang, F., and Li, B. (2018). Na$_2$Mn$^{3+}_{0.3}$Mn$^{4+}_{2.7}$O$_{6.85}$: A cathode with simultaneous cationic and anionic redox in Na-ion battery. Energy Storage Mater. 14, 361–366.

34. Shannon, R.D. (1976). Revised effective ionic radii and systematic studies of interatomic distances in halides and chalcogenides. Acta Crystallogr. 32, 751–767.

35. Sathiya, M., Ramesha, K., Rousse, G., Foix, D., Gonbeau, D., Prakash, A.S., Doublet, M.L., Hemalatha, K., and Tarascon, J.-M. (2013). High performance Li$_2$Ru$_{1-y}$Mn$_y$O$_3$ (0.2≤y≤0.8) cathode materials for rechargeable lithium-ion

batteries: their understanding. Chem. Mater. 25, 1121–1131.

36. Jiang, M., Key, B., Meng, Y.S., and Grey, C.P. (2009). Electrochemical and structural study of the layered, "Li-excess" lithium-ion battery electrode material Li[Li$_{1/9}$Ni$_{1/3}$Mn$_{5/9}$]O$_2$. Chem. Mater. 21, 2733–2745.

37. Wang, Y., Xiao, R., Hu, Y.S., Avdeev, M., and Chen, L. (2015). P2-Na$_{0.6}$[Cr$_{0.6}$Ti$_{0.4}$]O$_2$ cation-disordered electrode for high-rate symmetric rechargeable sodium-ion batteries. Nat. Commun. 6, 6954.

38. Kim, S., Aykol, M., Hegde, V.I., Lu, Z., Kirklin, S., Croy, J.R., Thackeray, M.M., and Wolverton, C. (2017). Material design of high-capacity Li-rich layered-oxide electrodes: Li$_2$MnO$_3$ and beyond. Energy Environ. Sci. 10, 2201–2211.

39. Seo, D.H., Lee, J., Urban, A., Malik, R., Kang, S., and Ceder, G. (2016). The structural and chemical origin of the oxygen redox activity in layered and cation-disordered Li-excess cathode materials. Nat. Chem. 8, 692–697.

40. Hamaguchi, M., Momida, H., and Oguchi, T. (2018). First-principles study on cathode properties of Li$_2$MTiO$_4$ (M = V, Cr, Mn, Fe, Co, and Ni) with oxygen deficiency for Li-Ion batteries. J. Phys. Soc. Jpn. 87, 044805.

41. Yabuuchi, N., Takeuchi, M., Nakayama, M., Shiiba, H., Ogawa, M., Nakayama, K., Ohta, T., Endo, D., Ozaki, T., Inamasu, T., et al. (2015). High-capacity electrode materials for rechargeable lithium batteries: Li$_3$NbO$_4$-based system with cation-disordered rocksalt structure. Proc. Natl. Acad. Sci. USA 112, 7650–7655.

42. Larson, C., and Von Dreele, R.B. (2004). General structure analysis system (GSAS). In Los Alamos National Laboratory Report LAUR, 86Los Alamos National Laboratory Report LAUR, p. 748.

43. Kresse, G., and Hafner, J. (1993). Ab initio molecular dynamics for liquid metals. Phys. Rev. B Condens. Matter 47, 558–561.

44. Kresse, G., and Hafner. (1994). Ab initio molecular-dynamics simulation of the liquid-metal–amorphous-semiconductor transition in germanium. Phys. Rev. B 49, 14251–14269.

45. Kresse, G., and Furthmüller, J. (1996). Efficiency of ab-initio total energy calculations for metals and semiconductors using a plane-wave basis set. Comput. Mater. Sci. 6, 15–50.

46. Kresse, G., and Furthmüller, J. (1996). Efficient iterative schemes for ab initio total-energy calculations using a plane-wave basis set. Phys. Rev. B Condens. Matter 54, 11169–11186.

47. Blöchl, P.E. (1994). Projector augmented-wave method. Phys. Rev. B Condens. Matter 50, 17953–17979.

48. Perdew, J.P., Ernzerhof, M.B., and Burke, K. (1996). Rationale for mixing exact exchange with density functional approximations. J. Chem. Phys. 105, 9982–9985.

49. Dudarev, S.L., Botton, G.A., Savrasov, S.Y., Humphreys, C.J., and Sutton, A.P. (1998).

Chem

Electron-energy-loss spectra and the structural stability of nickel oxide: an LSDA+U study. Phys. Rev. B *57*, 1505–1509.

50. Wang, L., Maxisch, T., and Ceder, G. (2006). Oxidation energies of transition metal oxides within the GGA+U Framework. Phys. Rev. B *73*, 195107–195112.

51. Yao, Z., Kim, S., He, J., Hegde, V.I., and Wolverton, C. (2018). Interplay of cation and anion redox in Li$_4$Mn$_2$O$_5$ cathode material and prediction of improved Li$_4$(Mn,M)$_2$O$_5$

electrodes for Li-ion batteries. Sci. Adv. *4*, eaao6754.

52. Yao, Z., Kim, S., Aykol, M., Li, Q., Wu, J., He, J., and Wolverton, C. (2017). Revealing the conversion mechanism of transition metal oxide electrodes during lithiation from first-principles. Chem. Mater. *29*, 9011–9022.

53. Hart, G.L.W., and Forcade, R.W. (2008). Algorithm for generating derivative structures. Phys. Rev. B *77*, 224115–224126.

54. Hart, G.L.W., and Forcade, R.W. (2009). Generating derivative structures from multilattices: algorithm and application to hcp alloys. Phys. Rev. B *80*, 014120–014127.

55. Hart, G.L.W., Nelson, L.J., and Forcade, R.W. (2012). Generating derivative structures at a fixed concentration. Comput. Mater. Sci. *59*, 101–107.

56. Michel, K.J., Zhang, Y., and Wolverton, C. (2013). Fast mass transport kinetics in B20H16: a high-capacity hydrogen storage material. J. Phys. Chem. C *117*, 19295–19301.